



# Effects of graphene and carbon coating modifications on electrochemical performance of silicon nanoparticle/graphene composite anode

Rhet C. de Guzman<sup>a</sup>, Jinho Yang<sup>b</sup>, Mark Ming-Cheng Cheng<sup>b</sup>, Steven O. Salley<sup>a</sup>, K.Y. Simon Ng<sup>a,\*</sup>

<sup>a</sup> Department of Chemical Engineering and Materials Science, Wayne State University, Detroit, MI 48202, USA

<sup>b</sup> Department of Electrical and Computer Engineering, Wayne State University, Detroit, MI 48202, USA

## HIGHLIGHTS

- Studied the effects of graphene and Si modifications in the battery performance.
- High rate cycles are possible with a good balance of graphene sheet size and disorder.
- Graphene with high pyridinic N resulted in both higher capacity and rate capability.
- PAN-based coating approach resulted in N-doped C coating on Si.
- Si with N-containing coating showed overall capacity retention and rate performance.

## ARTICLE INFO

### Article history:

Received 8 April 2013

Received in revised form

10 July 2013

Accepted 28 July 2013

Available online 3 August 2013

### Keywords:

Lithium ion battery  
Silicon nanoparticles  
Graphene  
Composite anode

## ABSTRACT

The effects of graphene and C coating modifications on electrochemical performance of silicon nanoparticle (SiNP)/graphene composite anode were investigated. Graphene with varying sheet sizes (238, 160 and 113 nm) were used as an anode material where a cycling performance dependence on the sheet size (edge sites and sheet disorder) was observed. Temperature-dependent N doping of graphene resulted in graphene with N (5.97% w/w) presenting three binding configurations: 72.1% pyridinic N, 22.4% pyrrolic N and 5.5% graphitic N. The nitrated graphene displayed improved cycling capacity and minimized performance decay, principally due to the pyridinic N. Galvanostatic cycling using increasing current density rates (500–2500 mA g<sup>-1</sup>) of SiNP composites with C coating/deposition showed improvements in both capacity retention and rate performance. A polyacrylonitrile (PAN)-based coating scheme was used to produce a N-containing (2.20%) C coating which displayed the best high performance improvements, attributable to the minimization of direct solid-electrolyte interphase (SEI) formation and improvement in the conduction path. Optimization of the methods to achieve the best modification characteristics might enable performance improvements that maximize the capabilities of the materials.

© 2013 Elsevier B.V. All rights reserved.

## 1. Introduction

The promise of greatly increased anode specific capacity for lithium ion batteries (LIBs), by as much as ten-fold through the substitution of Si (theoretical capacity of 3572 mAh g<sup>-1</sup> [1]) for graphite (theoretical capacity of 372 mAh g<sup>-1</sup> [2]), has tremendously influenced the direction of secondary battery research.

Likewise, Si's abundance and mature infrastructure further drive this cause. With Si, a high capacity Li alloying reaction produces a Li-rich phase (Li<sub>15</sub>Si<sub>4</sub>) compared with the intercalation reaction with graphite (LiC<sub>6</sub>). However, the increased accommodation of Li<sup>+</sup> during charge–discharge cycles induces large volume variations (as much as 370%) and stress on the bulk anode matrix that ultimately leads to failure. In view of this hindrance, different strategies have been pursued to mitigate this effect including: amorphous thin films [3–6], nanowires [7–9], nanotubes [10], and porous morphologies [11–13]. Despite these advances, capacity degradation during cycling is still problematic, suggesting electrode fracturing

\* Corresponding author. Tel.: +1 313 577 3805; fax: +1 313 577 8171.

E-mail address: [sng@wayne.edu](mailto:sng@wayne.edu) (K.Y. Simon Ng).

and delamination that leads to eventual electrical contact losses. The most promising recent advances have employed Si nano-sized particles coupled with carbonaceous material [14–22] as a form of support; however, this configuration is not without challenges.

Graphene is such a carbonaceous material that has great potential as a support. Its highly organized  $sp^2$ -bonded C atoms provide outstanding mechanical and electrical properties compared with other known materials [23,24]. It has the potential to assist in the electron conductivity in composite anodes while providing a matrix for the SiNPs. Lately, graphene has been widely used as an anode material that demonstrates capacities even higher than those of current state-of-the-art graphite. Such performance was achieved through the use of disordered graphene (containing imperfections) where Li can be hosted on both sides of the sheets [25,26]. However, increasing the level of disorder also increases the number of edge sites which promote side reactions leading to large irreversible capacity losses. These sites have been proven to be more electrochemically active than the basal plane sites, leading to more electrolyte decomposition [27]. This causes severe breakdown of commercially available electrolyte (e.g.,  $LiPF_6$  in organic solvents), forming an unstable non-conducting SEI [14,28]. Nitrogen has a stronger electronegativity compared with carbon; its lone pair electrons form conjugated bonds with the graphene  $\pi$ -system, hence it has been widely studied as a dopant to modify graphene's electronic and chemical properties [29,30]. Nitrogen doping of graphene anode materials has resulted in reversible capacities much higher than graphite [28,31]. While it shows much promise, it has not yet been explored in standalone graphene anode materials.

Nano-sized Si particles benefit from having high surface area, which provides more sites for Li alloying to improve electrode capacity (and rate capability). However this attribute also gives rise to intensive side reactions with the electrolyte (especially  $LiPF_6$  species) as reported by Aurbach et al. [32]. These side reactions are the primary source of SEI, which irreversibly consumes Li during formation and ultimately contributes to cell capacity fading. In order to address this, a predominant approach has been used to apply a C-based material to act as a passivation layer. This technique has been used in thin films [33] and clustered particles [15–17]. All have shown varying levels of improvement by minimizing side reactions with the electrolyte; yet it is still a challenge to achieve high cycle life. Employing a N-containing C coating on the SiNP [34,35] to further improve the electrochemical kinetics can potentially surpass plain C coated Si. Since the Li-rich alloying reactions are still the governing reactions with Si-based anode materials, full mitigation of the cycling volume expansion is very difficult to accomplish. Even though SiNPs have increased fracture toughness [36], volume variations are still considerable. Even for particles within the nanometer range, volume expansion (much worse fracturing) of particles due to cycling could lead to successive cycles of SEI rupture and reformation that will lead to further irreversible loss of Li (and capacity). To address these issues, the objective of this work is to explore modification schemes for the components of SiNP/

graphene composite anode in order to improve the cycling performance. The effect of graphene sheet size variation and the effects of nitriding level of standalone graphene anodes at varying temperatures on the charge–discharge performance of the resulting anode were investigated. The SiNP was subjected to C-based coating that is targeted to protect the particles from direct exposure to the electrolyte while improving the conduction network. This modification may potentially avoid the unstable cycle of SEI formation/reformation as the SiNPs are expected to expand. Furthermore, a novel N-containing coating using carbonized PAN was used as a coating material for highly dispersed SiNP. These modifications were coupled with an improved surfactant-assisted particle dispersion procedure that can create a well dispersed particle (and modified particles) within a graphene matrix. Overall, the resulting improvements in cycling performance brought by these modifications may contribute to the further advancement of SiNP-based composite anode design.

## 2. Experimental

### 2.1. Graphene modifications

#### 2.1.1. Graphene anode synthesis

Three sources of graphite (Table 1): graphite A (Dixon Microfyne, Ashbury, NJ), B (230U grade, Asbury Carbons, Asbury NJ) and C (2299 grade, Asbury Carbons) with varying flake sizes were used as the graphene precursor to make graphite oxide via a two-stage Hummers' method according to Kovtyukhova et al. [37]. In a series of steps, the graphites were first pre-oxidized and then subjected to strong oxidizing agents to produce the respective graphite oxides. After the Hummers' method proper, graphite oxide suspensions of about  $6 \text{ mg mL}^{-1}$  were stored in amber bottles at room temperature.

In order to create the graphene anode material, 6 mL of the graphite oxide suspensions were probe sonicated (Misonix, Ultrasonic Cell Disruptor, Farmingdale, NY, 100 W, 22.5 kHz) for 2 h. This step exfoliates the expanded structure of graphite oxide to form the graphene oxide (GO) platelets. All sonics-based steps were performed at room temperature and were closely monitored to minimize temperature increase. The samples were then vacuum-filtered (setup: Millipore 47 mm all-glass vacuum filter holder-funnel and flask; filter:  $0.2 \mu\text{m}$  pore, Whatman Anodisc) forming solid GO papers. The resulting structures were then air-dried overnight followed by thermal reduction. The reduction was done in a tube furnace (Series 3429, Applied Test Systems Inc., Butler, PA) using 10%  $H_2$  in Ar at  $100 \text{ mL min}^{-1}$  and  $700^\circ\text{C}$  for 1 h, from which graphene A, B and C were obtained.

#### 2.1.2. Graphene anode nitriding

After the GO paper was dried overnight, GO A was then nitrided inside a tube furnace. Two temperatures ( $800$  and  $950^\circ\text{C}$  for 2 h) were used with an  $NH_3$  (anhydrous, Cryogenic Gases, Detroit, MI) atmosphere to reduce and, at the same time, to incorporate N on

**Table 1**  
DLS sheet size and BET surface area measurements for the three different graphite sources and the resulting graphenes.

Sample	Graphite			Graphite oxide		Resulting graphene (powder)		Graphene anode (film)
	Source	Description	Surface area (BET)	Sheet size (DLS)	Sheet size (DLS)	Surface area (BET)	Surface area (BET)	
A	Dixon Microfyne	44 $\mu\text{m}$ Graphite Flakes	$3.07 \text{ m}^2 \text{ g}^{-1}$	$1266 \pm 33 \text{ nm}$	$238 \pm 2 \text{ nm}$	$172 \text{ m}^2 \text{ g}^{-1}$	$25.1 \text{ m}^2 \text{ g}^{-1}$	
B	Asbury 230U	15 $\mu\text{m}$ Graphite Flakes	$5.28 \text{ m}^2 \text{ g}^{-1}$	$542 \pm 14 \text{ nm}$	$160 \pm 4 \text{ nm}$	$380 \text{ m}^2 \text{ g}^{-1}$	$48.3 \text{ m}^2 \text{ g}^{-1}$	
C	Asbury 2299	0.25–5 $\mu\text{m}$ nano-Graphite powder	$342 \text{ m}^2 \text{ g}^{-1}$	$209 \pm 3 \text{ nm}$	$113 \pm 3 \text{ nm}$	$419 \text{ m}^2 \text{ g}^{-1}$	$58.2 \text{ m}^2 \text{ g}^{-1}$	

the resulting graphene structure. The nitrated graphene anodes were denoted as GwN800 and GwN950. The nitrated graphene anodes were compared with the performance of the control graphene anode (graphene A) which was obtained from the reduction using  $H_2$ .

## 2.2. Nano-Si modification

SiNP with a size distribution of 5–10 nm, were acquired from Meliorum Nanotechnology (Rochester, NY). The particles were stored in an Ar-filled glovebox with  $O_2$  and moisture content <1 ppm. Prior to modifications, desired amount of particles were carefully transferred to ceramic boats and then loaded into the tube furnace, taking care to prevent any contamination of the particles. The tube was purged with the reaction gas for 30 min before starting any heating to reach the target temperature.

### 2.2.1. Carbon deposition on SiNPs

In order to deposit C on the particles (CdepSiNP), a feed of acetylene ( $80 \text{ mL min}^{-1}$ ) and Ar ( $160 \text{ mL min}^{-1}$ ) gases was used in a tube furnace at a reaction temperature of  $500^\circ\text{C}$  for 2 h as reported [14,38].

### 2.2.2. Carbon coating of SiNPs

Two different C coating schemes were used to produce a (1) casing and a (2) N-containing coating of the SiNPs. The C casing traps multiple particles and was prepared similar to the precursor structure of [39]. A batch of 100 mg of SiNP was pressed into a 12 mm (diameter) disk and then was placed in a ceramic boat where it was covered (top and bottom) by a total of 1 g of polyvinyl chloride powder (PVC, PolySciences Inc., Warrington, PA). The whole sample was placed within the tube furnace, which was purged and then heated to  $300^\circ\text{C}$  under  $N_2$  (ultrahigh purity, Cryogenic Gases) for 2 h. At this state the PVC melt is expected to penetrate the disk and fill the voids [39]. In the same environment, the melt was then carbonized at  $900^\circ\text{C}$  for 2 h, resulting in a C–Si composite disk. The composite disk was ground back to powdered form and designated as CoatASiNP.

For the N-containing coating of the SiNP, a PAN (PolySciences) solution was first prepared by dissolving 50 mg of PAN in 25 mL of N-methyl pyrrolidone (NMP, Sigma Aldrich, St. Louis, MO). Then, 15 mg of SiNP were dispersed in the solution by probe sonication for 1 h, and then stirred overnight. The wet sample was collected by centrifugation and then dried at  $80^\circ\text{C}$  under vacuum. The carbonization was performed similarly to the procedure of Zhu et al. [40], where the dried powder was placed in a tube furnace and then subjected to  $270^\circ\text{C}$  for 30 min to stabilize the coating while in a  $N_2$  atmosphere. Then, after cooling down to room temperature, the coating was carbonized by heating to  $900^\circ\text{C}$  for 2 h, thus achieving CoatBSiNP.

## 2.3. Composite anode formation

The modified particles were weighed and then dispersed using a surfactant-enhanced technique to achieve good particle dispersion. The particles were first placed in methanol and probe sonicated for 15 min; afterward n-octyl alcohol (99%, Across Organics, NJ) was added to achieve a 1% (v/v) content and then the mixture was subjected to an additional 45 min of sonication. In order to test the modified particles, a standalone composite anode (no binder and conductive additives was added) was formed with graphene A using procedures as outlined by Lee [15]. A suitable amount of graphite oxide A was added to the particle dispersions in order to get 1:1 weight ratio (Si:C) after which the samples were sonicated for 2 h. In this step, the sonics exfoliate the expanded structure of

graphite oxide to form the GO platelets while at the same time dispersing the modified SiNPs. The formation and reduction steps followed (identical to the graphene anode procedure) where the 3 samples were produced: CdepSiNP/Graphene, CoatASiNP/Graphene and CoatBSiNP/Graphene anodes. The standalone composite materials were sampled, weighed and prepared for testing.

## 2.4. Cell assembly

The cells were assembled in a CR2032 type button cell, loaded typically with  $\sim 0.5 \text{ mg}$  of the anode material: graphene ( $1 \text{ mg cm}^{-2}$ ,  $25 \mu\text{m}$  thick) or composite ( $2 \text{ mg cm}^{-2}$ ,  $5\text{--}10 \mu\text{m}$  thick). The anode acts as the cell's working electrode with the Li metal (99.9%,  $0.75 \text{ mm}$  thick, Alfa-Aesar) acting as both counter and reference electrode (half-cell configuration). A pre-prepared solution of  $1.0 \text{ M LiPF}_6$  dissolved in ethylene carbonate (EC)/dimethyl carbonate (DMC) 1:1(v/v) solution from Novolyte technologies (Independence, OH) was used as the electrolyte. The cells were assembled and crimp sealed in an Ar-filled glovebox.

## 2.5. Characterization

Scanning electron microscopy (SEM, JSM-6510LV-LGS at 25 kV) and field emission SEM (FESEM, JSM-7600F at 15 kV) were used to get high magnification micrographs. Transmission electron microscope (TEM) micrographs were acquired on a JEOL-2010 FastEM at 200 kV. Chemical composition analysis was done using the equipped Energy Dispersive X-ray Spectrometer (EDS). Graphene sheet size measurements were done using a Zetasizer Nano-ZS (Malvern Instruments, Worcestershire, United Kingdom) dynamic light scattering (DLS) unit. The non-invasive back scattered light was detected at an angle of  $173^\circ$ , platelet size was calculated via a CONTIN analysis and presented as the z-average size. Reported sizes were the average of three measurements from three separate sampling. In order to identify the graphene materials, Raman spectra were recorded using Triax 550 (Horiba Jobin Yvon, Edison, NJ) with a 514 nm laser excitation. Brunauer–Emmett–Teller (BET) surface area measurements were performed using a Micrometrics model ASAP 2010 surface area analyzer (North Huntingdon, PA) with  $N_2$  as the analysis gas. Samples were degassed at  $150^\circ\text{C}$  for 6 h to prior the analysis to remove any adsorbed molecules. X-ray photoelectron spectroscopy (XPS) analysis was conducted with a PHI 670 Scanning Auger Nanoprobe (Physical Electronics, Chanhassen, MN) at 220 W X-ray power to further investigate the binding characteristics of the samples' composition. A survey scan was first initiated and then high resolution multiplexes on each element of interest with 23.5 eV pass energy was performed.

## 2.6. Electrochemical measurements

Electrochemical cycling of the assembled cells was performed galvanostatically with a cut-off voltage range of 0.01–1.5 V. For the graphene samples, a constant current density of  $150 \text{ mA g}^{-1}$  was applied for the first 40 cycles. After this step, varying densities of 300, 750, and  $1500 \text{ mA g}^{-1}$  were used after every 10 cycles to assess the rate performance of the cells. The cells were then cycled back to a current density of  $150 \text{ mA g}^{-1}$  in order to measure the changes in capacity following previous high current density cycles. The composite anodes containing the modified SiNP were subjected to a similar cycling regimen but with higher densities:  $500 \text{ mA g}^{-1}$  for the first 40 cycles, then 900, 1,500, 2500 and finally back to  $500 \text{ mA g}^{-1}$  after every 10 cycles. The baseline performance of the particles was evaluated using a composite anode containing pristine SiNP (without any modifications). The electrochemical cycling tests were done using a Gamry (Warminster, PA) Reference 3000,

Gamry series G 300 or a Maccor (Tulsa, OK) Series 4200 cycler. Electrochemical impedance spectroscopy (EIS) measurements were performed using a Parstat 2273 with an AC voltage amplitude of 5 mV in the frequency range of 0.1–100,000 Hz. All electrochemical tests were performed at room temperature and only after the open circuit potentials were stable.

### 3. Results and discussion

#### 3.1. Graphene modifications

##### 3.1.1. Graphene sheet size variation

Fig. 1a–c show the relative size variation of the graphite flakes. From the SEM images, the flake sizes of graphite A > graphite B > graphite C, which is consistent with the properties summarized in Table 1. Upon conversion of the graphite to graphene, the same size relationship still holds (Fig. 1d–f). DLS data (Table 1) were

collected during the dispersion stages of the graphene preparation: graphite oxide (after Hummers' method) and GO (after sonication). Between the two stages there is a substantial decrease in the measured sheet size indicating that the sonication is responsible for both exfoliating the graphene sheets and reducing the size of the platelets. The DLS average sheet size measurements of the GO precursors are  $238 \pm 2$  nm (graphene A),  $160 \pm 4$  nm (graphene B) and  $113 \pm 3$  nm (graphene C). The measurements suggest that the graphene anodes formed from these will have 3 distinct sheet sizes with a variation of around 60 nm. Once formed into the graphene anode, the graphene sheets were stacked together to form the anode material. The results indicate that the smaller the graphene sheet size, the more disordered the sheets become, the rougher surface and hence a higher BET surface area was observed.

Raman profiles (Fig. 2) of the graphene anodes are very similar with each other and are comparable to those that exhibit defects [41]. The spectrum of graphene A (Fig. 2a) displays a G band

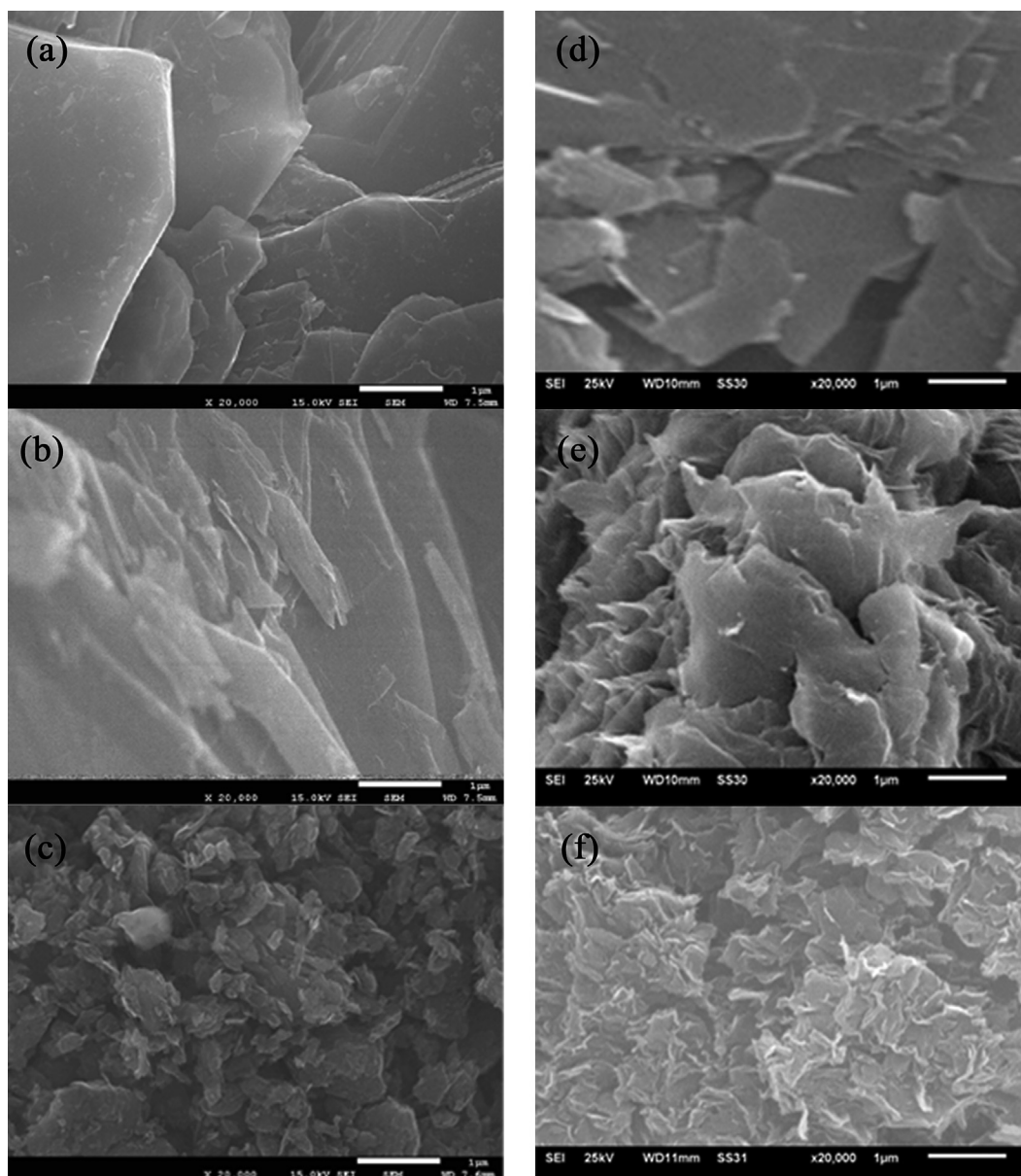


**Fig. 1.** FESEM images of the graphite flakes of source (a) A, (b) B and (c) C. SEM micrographs detailing the decrease in sheet size and the expansion brought by the Hummers' method on graphene (d) A, (e) B and (f) C. Scale bars are all 1 µm.

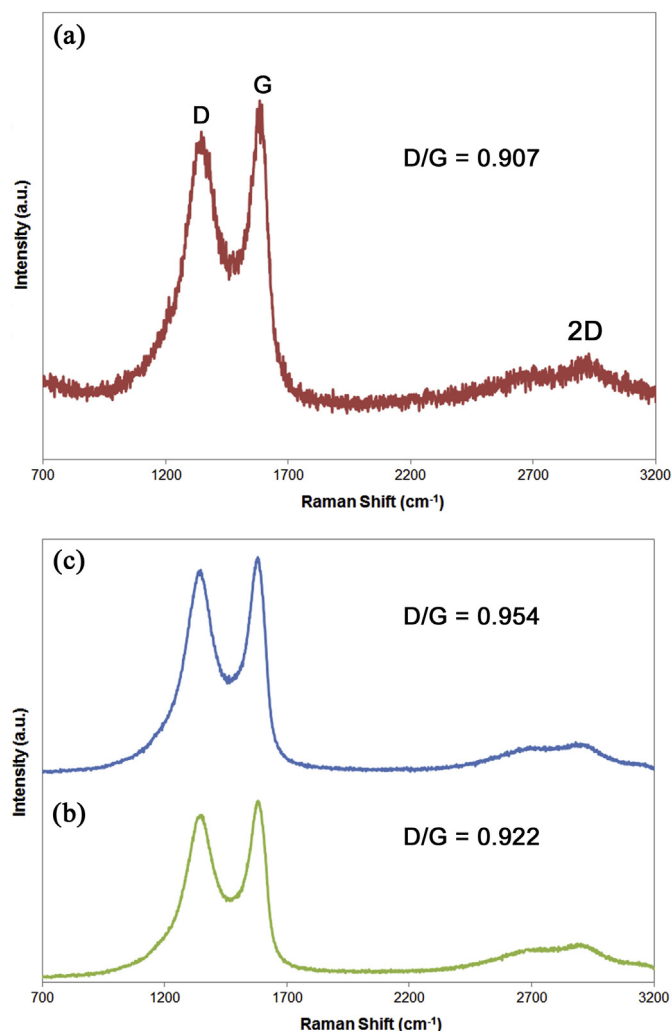


Fig. 2. Raman spectra of the graphene anodes (a) A, (b) B and (c) C.

( $1580\text{ cm}^{-1}$ ) for  $\text{sp}^2$  domains and a D band ( $1330\text{ cm}^{-1}$ ) relating edge planes and disordered structures [42]. Both graphenes B and C (Fig. 2b–c) exhibited the same bands at the same Raman shifts. Since these three anodes differ in sheet/platelet sizes, the resulting edge planes and disorder are also affected. Closer examination of the ratios between the intensities of the D and G bands (D/G) indicate that the smaller the sheet sizes the more edge sites and disorder it creates, which increases the D/G ratio.

Prior to reduction, EDS analyses (in agreement with XPS data) show that GOs have similar compositions: 66% (w/w) C and 33% O (<1% trace: Al, Cl, N and S). After the reduction step forming graphene, 7.7% O (92% C and <1% trace: Al, Cl, N and S) is still retained, implying that few  $\text{sp}^3$ -hybridized C atoms are recovered back into an  $\text{sp}^2$ -hybridized state [16]. This retains distortions in the graphene morphology and warps/folds are evident as in Fig. 1d–f. These graphene characterizations clearly indicate that the samples are nearly identical with each other except for the intended difference in sheet/platelet size.

The potential profiles of the graphenes during cycling are presented in Fig. 3a. The accommodation of  $\text{Li}^+$  (lithiation) into the working electrode characterized by the drop of potential compared with  $\text{Li/Li}^+$  is identified as the charge reaction; while the release of  $\text{Li}^+$  (delithiation, increase in potential) is called the discharge. The profiles are very similar to the observed graphene cycling reported

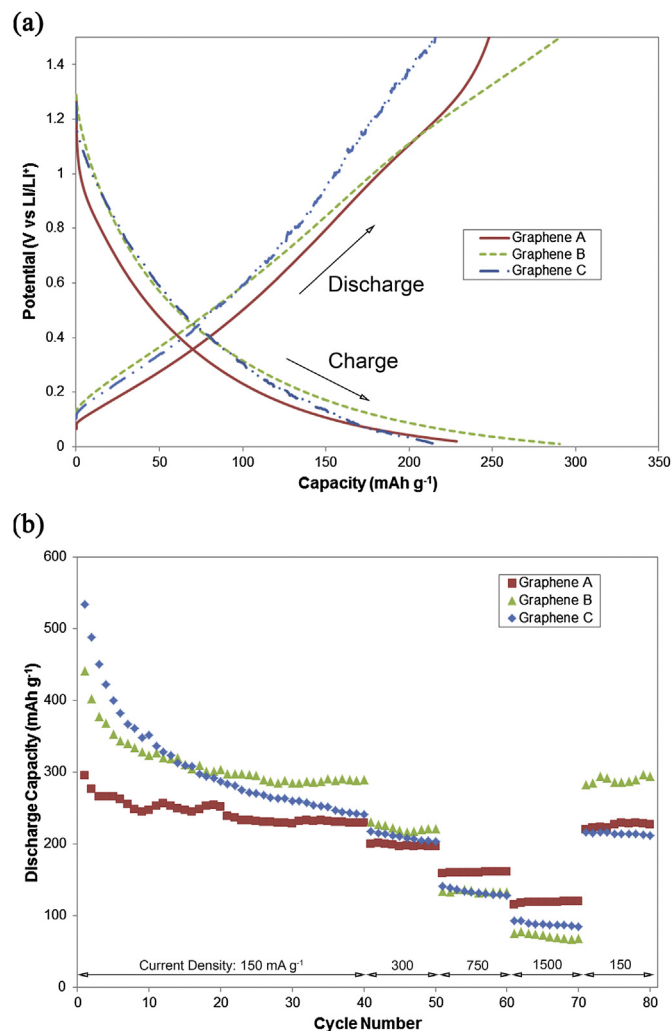


Fig. 3. (a) Charge–discharge profiles of graphene A, B and C using  $150\text{ mA g}^{-1}$ . (b) Cycling performance using various current densities.

by others [26,42,43]. Between the three, the slope of the charge–discharge curve increases with the decrease in sheet size, which can be attributed to the edge type intercalation mechanism as suggested by Yoo et al. [43], a type that is not as stable as the intercalation in graphite. The relative amount of observed edges in Fig. 1d–f, and the increase in D/G ratio of the Raman spectra (Fig. 2) [26] correlate well with the observed trend.

The cycling performance of graphene A, B and C is shown in Fig. 3b. Due to the highest level of sheet disorder and BET surface area in graphene C, the initial discharge capacity is the highest. Graphene C exhibits first discharge capacity of  $530\text{ mAh g}^{-1}$  which is 80 and 20% higher than graphene A and B, respectively. However, the rate of decay in capacity of C with cycling is substantial, only retaining 45% of its initial capacity (82% for A and 65% for B) after 40 cycles at the low rate ( $150\text{ mA g}^{-1}$ ). The highest specific surface area of graphene C is expected to also produce the highest amount of SEI, and thus higher resistance and conversely greatest losses of capacity [44]. Likewise, the large capacity fading can also be attributed to the edge sites that are capable of catalyzing the breakdown of electrolytes [28,45]. Graphene B shows the best capacity displayed after 40 cycles ( $285\text{ mAh g}^{-1}$ ). However, during the higher rates of cycling, graphene B, as well as C performed poorly compared with A ( $120\text{ mAh g}^{-1}$ ). For higher current densities, it is expected that shorter diffusion path (from shorter/smaller

graphene sheets) should yield better high rate dischargeability [25]. Interestingly, the observed performance was the contrary. A possible explanation for this can be attributed to surface SEI formation of graphenes. SEI progressively forms with increasing charge/discharge cycles, and with higher surface area (higher edge sites). Due to the non-conducting nature of the SEI, the material resistance has more pronounced effects as higher rates are used. Overall, fast charge and discharge are hindered. EIS measurements in Fig. 4 support this claim. At the early part (cycle 5) of cycling (Fig. 4a), the semicircle part (charge transfer resistance) and the sloped straight line (diffusion resistance through the bulk material) of the Nyquist plot are both lower for the graphene C, which coincides with the higher discharge capacity. After further cycling to the 70<sup>th</sup> run, where the cell has been subjected to  $1500 \text{ mA g}^{-1}$ , both charge transfer and diffusion resistances are higher in graphene C than in A (Fig. 4b), indicating unsuppressed SEI formation [46] that increases the anode resistance and impedes the electrochemical kinetics (rate performance). These findings indicate that electrochemical performance of a graphene anode is highly dependent on the graphene sheet size; and a balance of performance can be attained through size optimization.

### 3.1.2. Graphene anode nitriding

The elemental compositions from XPS of the source and nitrided graphenes are summarized in Table 2. Increasing the reaction

**Table 2**

XPS elemental composition of control and nitride graphene anodes, with N1s binding configuration quantities.

Element	Graphene	Graphene with N	
		Graphene A	
		GwN800	GwN950
		Wt %	Wt %
C 1s		92.07	90.70
O 1s		7.73	4.84
N 1s		—	4.46
N 1s	Pyridinic N	—	52.40
Configuration	Pyrrolic N	—	42.20
	Graphitic N	—	5.40

temperature where the GO was both reduced and doped with N resulted in the following: 4.46% (3.9 at%) for  $800^\circ\text{C}$  and around 5.97% (5.2 at%) for  $950^\circ\text{C}$ . The Raman spectra of both nitrided graphenes (Fig. 5) are similar with that of graphene A. With the introduction of N into the graphene structure, the D band intensity became greater than that of the G band similar to [28,29]. The increase in N content showed increasing D band intensity; the D/G ratio increased from 0.907 (graphene A), then 1.02 (GwN800) and finally 1.06 (GwN950). This suggests that the increase in N content brings about an increase in the degree of disorder/defects in the graphene sheets.

The charge–discharge curves in Fig. 6a for both the control and GwN800 present similar steep profiles. The trends of GwN950, especially the discharge, reflect more stable curves. The curve steepness can be attributed to electrochemical kinetics such as high SEI impedance or low internal diffusion of charge [28]. In Fig. 6b, there is a very clear distinction between the cycling performances of GwN950 vs. GwN800 and the graphene A. For the first cycle at  $150 \text{ mA g}^{-1}$ , GwN950 ( $\sim 500 \text{ mAh g}^{-1}$ ) displays as much as 66% higher capacity than the control. The stable capacity of GwN950 after 40 cycles is  $360 \text{ mAh g}^{-1}$ , at least a 40% improvement over the other preparations. At the highest current density ( $1500 \text{ mA g}^{-1}$ ), GwN950 was demonstrated to reversibly cycle around 58% of its stable capacity in the  $150 \text{ mA g}^{-1}$  runs ( $210 \text{ mAh g}^{-1}$ ), while GwN800 show only 41%. In order to gain a better understanding of the improved rate capability of GwN950, EIS measurements were performed at different cycling points as summarized in Fig. 7. During the first cycle (Fig. 7a); all three charge transfer resistances were the same. When the materials were subjected to higher currents corresponding to cycles 60 (Fig. 7b) and 70 (Fig. 7c), the

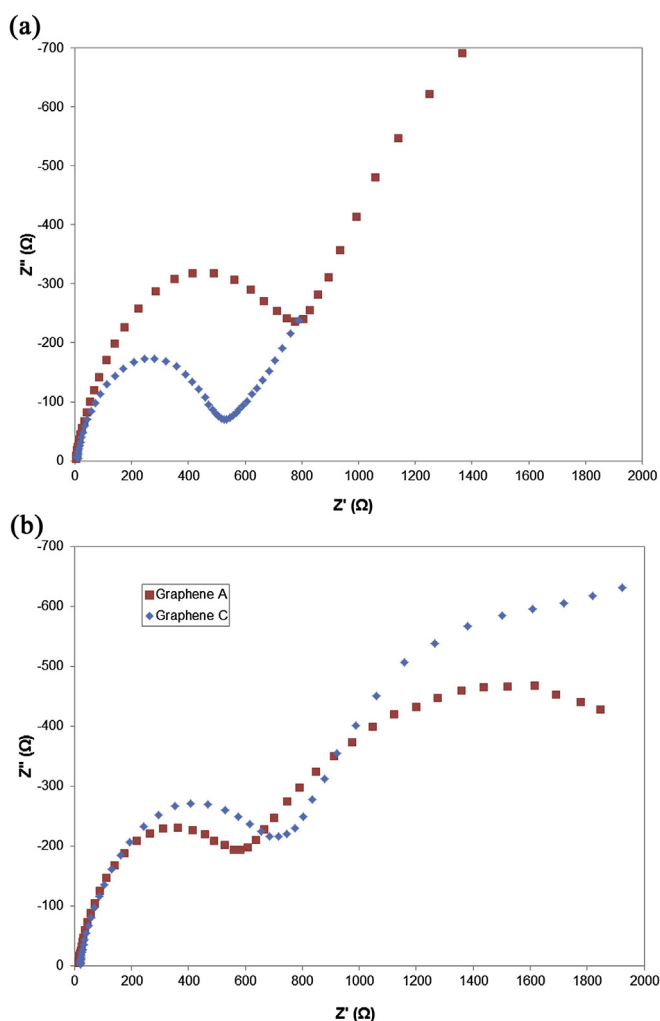


**Fig. 4.** Nyquist plots for graphene A and C after (a) cycle 5 and after (b) cycle 70.

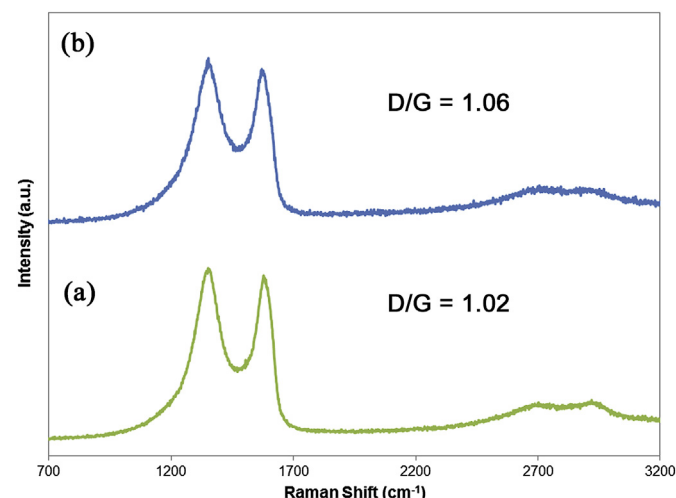


**Fig. 5.** Raman spectra of the nitrided graphene anodes: (a) GwN800 and (b) GwN950.

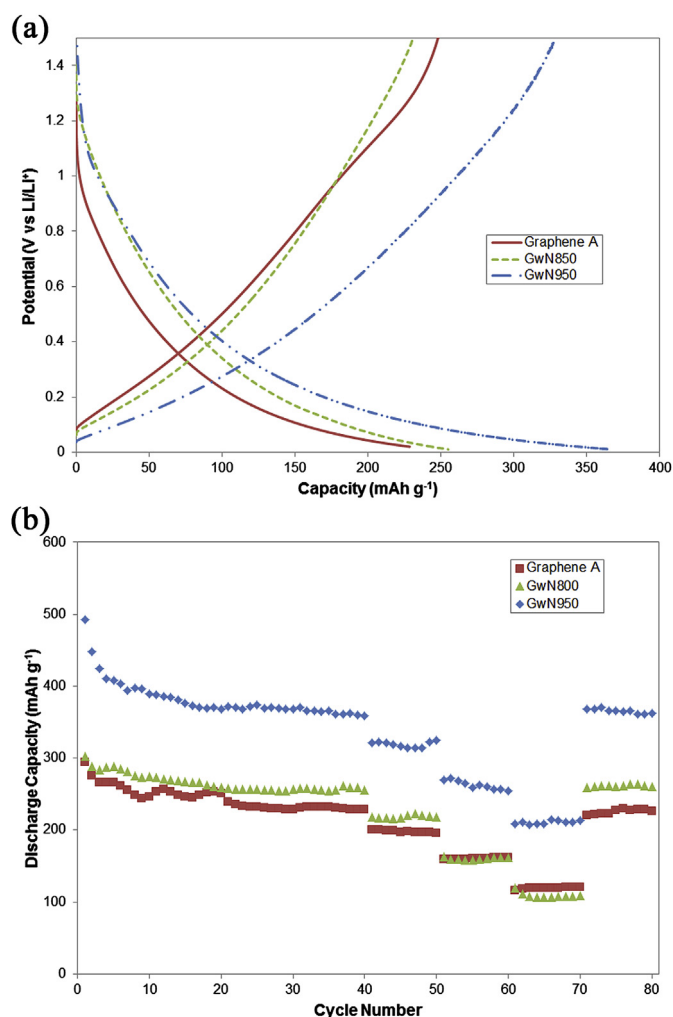


**Fig. 6.** (a) Charge–discharge profiles of graphene A, GwN800 and GwN950 using 150 mA g<sup>-1</sup> current loading. (b) Cycling performance of the nitride graphene samples using various current densities.

charge transfer resistances of GwN950 were the lowest, those of the control graphene and GwN800 did not present much difference from each other. These observations suggest the formation of a more stable SEI in the GwN950 sample. After cycle 70, back to using 150 mA g<sup>-1</sup>, all three anode materials recovered their respective cycle 4 discharge capacities. Based on the potential profiles and the cycling performances, it appears that the amount of N in GwN800 is not sufficient to provide considerable improvements to the electrochemical performance of the anode material while the amount in GwN950 is. However, the N contents of these two samples appear too close to be of significant bearing, thus warranting further investigations. XPS spectrum in Fig. 8 is used to analyze the binding configurations in the nitrated samples. Detailed analysis of the high resolution spectra of the N 1s (Fig. 8 inset) revealed three peaks: pyridine-like N (397.9 eV), pyrrole-like N (400.5 eV) and graphitic N (402.2 eV). These three forms/configurations of N binding have been well discussed in literature, with the pyridinic type being the most favorable for Li cycling [28,31,47]. Pyridinic N consists of two coordinate N atoms on the edges of hexagonal graphene with a filled lone-pair orbital forming the trigonal sp<sup>2</sup> structure [31,48]. This specific formation creates C vacancies on the graphene network [49] that are capable of holding more Li<sup>+</sup> than the pristine graphene structure, hence producing higher capacity output [31,47,50]. Aside from this, first-principle

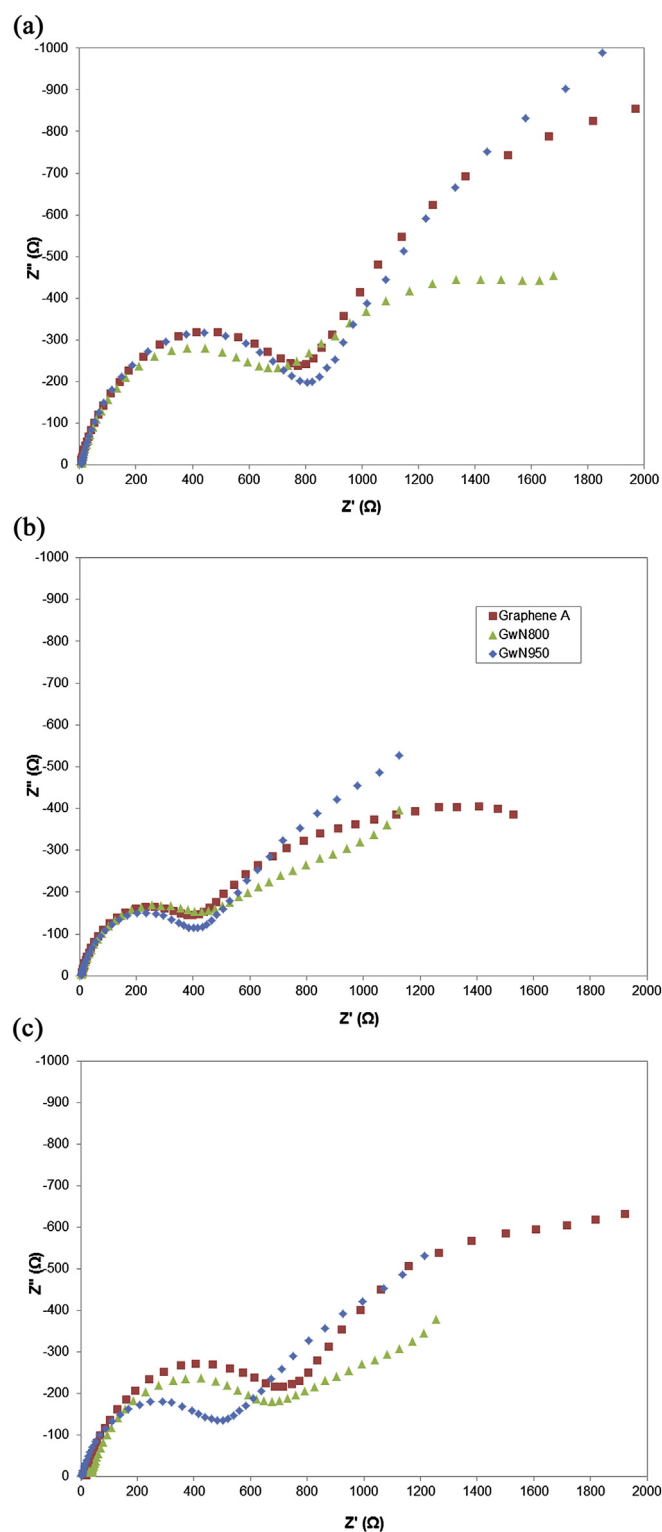


**Fig. 7.** Nyquist plots for graphene A, and the nitrated samples after (a) cycle 1, after (b) cycle 60 and after (c) cycle 70.

studies [47] have indicated that the resulting defect by the pyridinic N creates strong binding energies with Li, promoting stable Li hosting. Likewise, geometrical computation and optimization of the adsorbed Li<sup>+</sup> revealed that there is a low possibility of Li cluster formation that is very detrimental to the capacity. Overall,

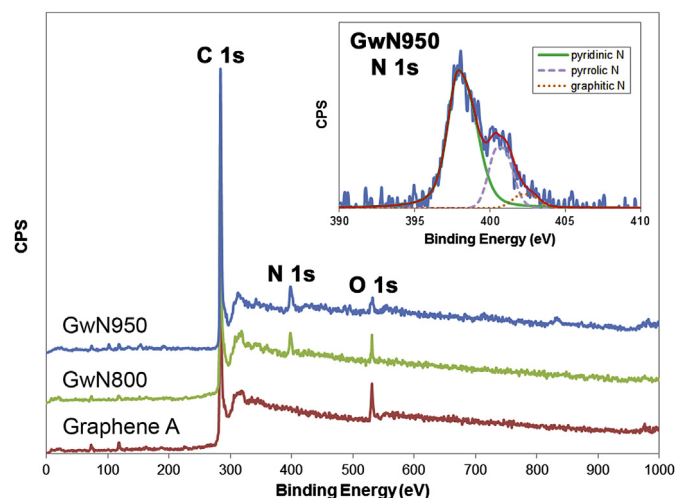


Fig. 8. XPS spectra of graphene A, GwN800 and GwN950. Inset: High resolution N 1s spectra of GwN950.

graphene with pyridine-like N is being viewed as the most suitable for Li storage, as compared with pyrrole-like N, graphitic N and pristine graphene. Curve fittings similar to that of in Fig. 8 (inset) were used to quantify the bearing of N binding configurations (Table 2). Pyridinic N of 52.4% and 72.1%, pyrrolic N of 42.2% and 22.4%; and graphitic N of 5.4% and 5.5% were measured for the GwN800 and GwN950, respectively. From these data, it is evident that GwN950 has substantially higher pyridinic N than GwN800, with a relative difference of about 20 units. Interestingly, the same difference is noticeable in the pyrrolic N values; with GwN800 having much more than GwN950. These results, and the increased overall N content, account for the significantly better performance of GwN950 over GwN800. From the N configuration differences, the only variable in the preparation of the nitrated samples is the reaction temperature, indicating that the annealing temperature has a significant effect on the amount of N doping and its configuration: the desired pyridinic N form is formed using higher temperature annealing. Corroborating the Raman observations in Fig. 5, the increase in N doping did indeed increase the degree of disorder in the graphene sheets through the resulting defect (and disordered carbon) mainly by vacancies when dopant N is introduced.

The introduction of N creates topological variations on the graphene layer, providing more active sites for Li storage (increased capacity). It also improves the conductivity of the C layer and charge transfer at the interface [51]. Likewise, it appears that the catalytic breakdown of the electrolyte at the graphene edge sites may be reduced by N doping to promote stable interfaces [28]. From the two sets of graphene modifications, GwN950 is the overall better anode. In order to get the best performance improvements, future optimizations studies are needed. Nonetheless, the findings of nitrating experiments solidified the hypothesis that N-containing C materials can enhance electrochemical performance. These results will be the basis of part of subsequent study on SiNP modifications.

### 3.2. SiNP modifications

#### 3.2.1. Carbon deposition on SiNP

String-like deposits of C trapped SiNPs producing the CSiNP as shown in Fig. 9a. TEM examination in Fig. 9b shows that SiNPs are loosely contacted by the C strands. EDS analysis reveals that the composition of CdepSiNP/graphene are as follows: 51% Si, 3% O and 46% C (w/w). The resulting electrochemical performance as

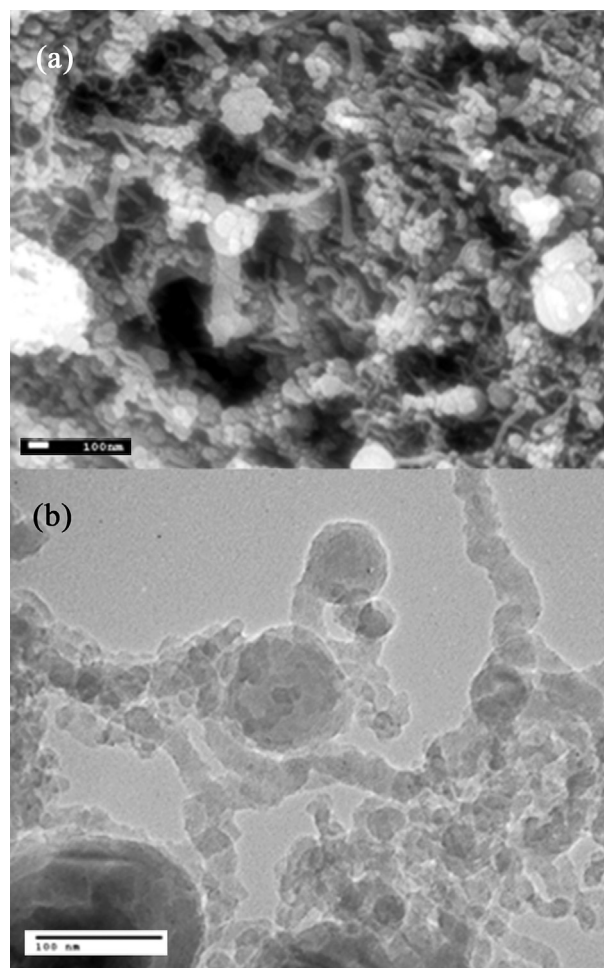


Fig. 9. (a) SEM image of the CSiNPs indicating spherical SiNPs and string-like C deposits. Close examination of the particles using (b) TEM shows loose C in contact with the particles. Scale bars are 100 nm.

compared with a composite anode made from bare SiNP and with a pure Si anode [16] is detailed in Fig. 10. From the first discharge, the composite with CSiNP showed a capacity of  $2426 \text{ mAh g}^{-1}$ , a 15% improvement compared with the composite using plain SiNP

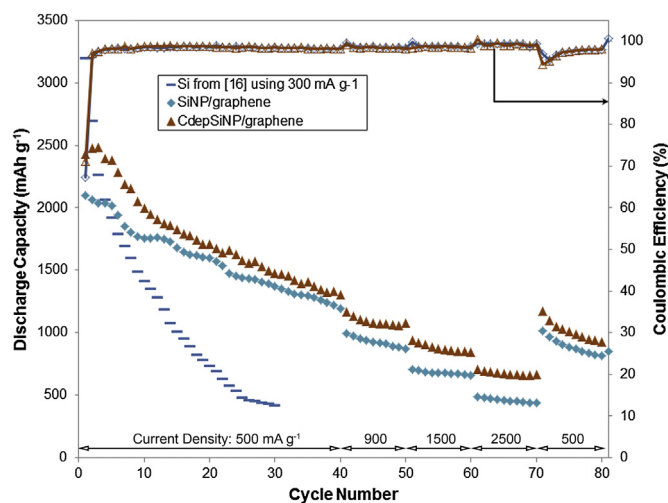
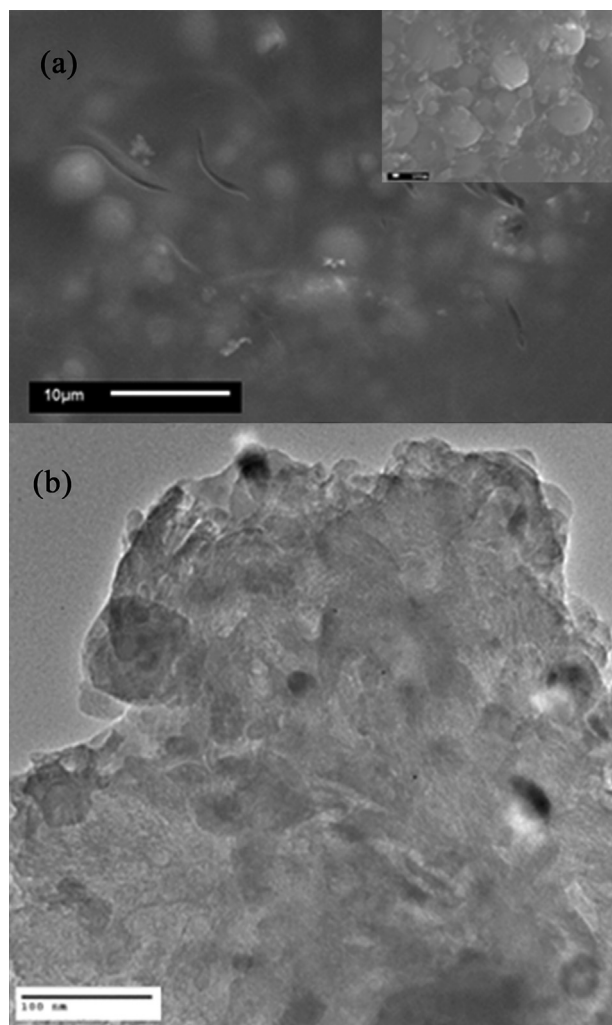
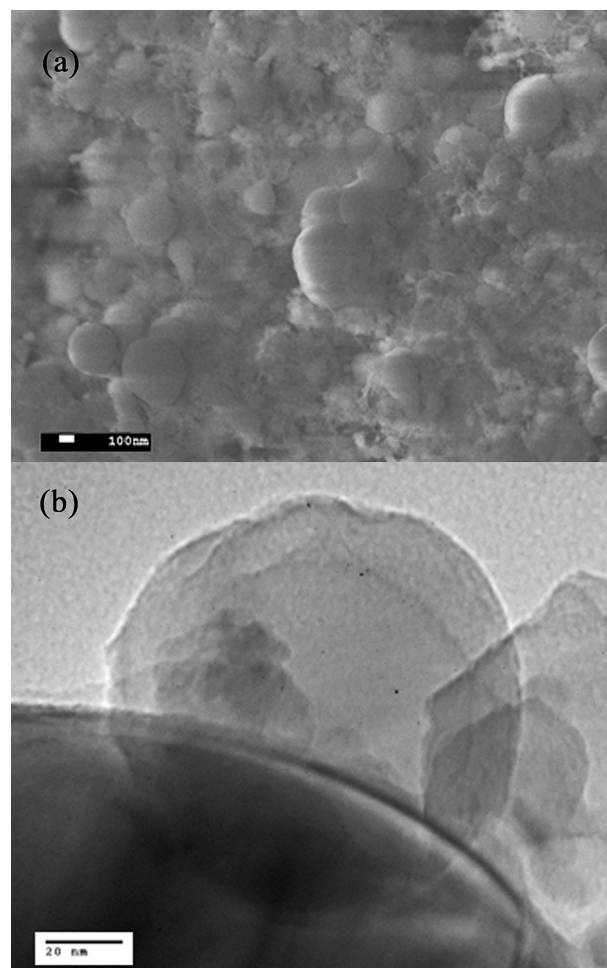


Fig. 10. Cycling performance of CdepSiNP/graphene, compared with the unmodified particle and Si [16].



**Fig. 11.** (a) FESEM image of CoatASiNP showing the trapped particles. Inset: Particle details, scale bar is 100 nm (b) TEM image of the structure showing predominant C coating.

(2100 mAh g<sup>-1</sup>). The Coulombic efficiency of CSiNP/graphene likewise presents a slight improvement compared with SiNP/graphene (71% vs. 67%). These results validate that amorphous C deposits/coatings of CdepSiNP can function as supplementary Li intercalation sites that can contribute to increase the capacity, as well as possibly forming a more stable SEI that reflects a relatively higher efficiency. Going towards the 40<sup>th</sup> cycle (using 500 mA g<sup>-1</sup>) the capacity improvement of C deposition was about 8%, displaying almost the same discharge as that of the control. At this point since the C deposits do not completely cover the particles; the SiNPs are exposed like the particles in the control to react with the electrolyte forming new unstable SEI (apart from the ones formed with the C deposits). With the volume expansion of the particles caused by cycling, contact losses and unstable formation of the SEI results in the high cycling resistance which manifests into the capacity decay. During the higher rate discharges (900, 1500 and 2500 mA g<sup>-1</sup>), it is clearly evident that the CdepSiNP/graphene displays a better rate performance. Although the magnitude is small, the relative improvement is as much as 50% greater than that of the SiNP/graphene anode (for 2500 mA g<sup>-1</sup> current density). This can be attributed to the improved conduction path brought by the loose C deposits.



**Fig. 12.** (a) FESEM image of the bulk phase of CoatBSiNP showing the coated particles. (b) TEM image of a particle and the resulting C coating.

### 3.2.2. Carbon coating of SiNP

Two approaches to provide a close contact with the particles were investigated: C casing coating and a N-containing C coating. Fig. 11a shows that the SiNPs are fully encased in carbonized PVC pitch before the Si/C composite disk was ground to μm ranged bits. Fig. 11a inset and b show that the coating effectively covers/traps small SiNPs clusters within an interconnected C casing material. On the other hand, the second coating fully covers the (individual) particles, resulting in CoatBSiNP as seen in Fig. 12a. Close up examination of one of the coated particles (Fig. 12b) shows an external coating (<5 nm thickness) that is homogeneously conforming to its shape. Table 3 summarizes the computed surface composition of the modified particles. Data here were acquired using the particles before any reduction step was performed, as evidenced by the high oxygen content of the particle surface. Nonetheless, the compositions are on par with what are expected. CoatASiNP demonstrates high C concentration with a noticeable decrease in oxygen and Si content (compared to the control), indicating a thick over layer of carbon. The small C composition indicates that CoatBSiNP is relatively thin. The most important aspect of these data is the successful inclusion of 2.20% N on the CoatBSiNP particles' surface. The retention of N from carbonized PAN is highly temperature dependent [34], PAN cyclizes and dehydrogenates on heating to form extended belts of fused pyridine rings [35]. High resolution XPS spectra of the N 1s peak in Fig. 13 reveal that the binding configurations with C are similar to those

**Table 3**

XPS elemental composition of the coated SiNPs before the reduction step, with the quantification of N1s binding in CoatBSiNP.

Element		SiNP	Coated SiNP	
		Control	CoatASiNP	CoatBSiNP
		Wt %	Wt %	Wt %
C 1s		0.37	32.50	17.10
O 1s		40.60	28.27	26.80
N 1s		—	—	2.20
Si 2p		59.03	39.23	53.90
N 1s Configuration	Pyridinic N	—	—	63.20
	Pyrrolic N	—	—	20.20
	Graphitic N	—	—	16.60

of nitrated graphene: pyridinic N, pyrrolic N and graphitic N. From the PAN carbonization, the resulting binding is mostly pyridinic in nature (63.2%).

After integrating the coated particles within the graphene A matrix to form the composite anodes, the cycling and rate performances were tested and presented in Fig. 14. The performance of the CoatASiNPs composite is inferior compared to the control anode. At first discharge, an almost identical value to the control was displayed at  $\sim 2100 \text{ mAh g}^{-1}$ , although the cycling efficiency is at 37% compared to 67% of the baseline composite. Also, the computed efficiency of CoatASiNP appears to be gradually increasing, achieving the value of the control ( $\sim 99\%$ ) only after 20 cycles. CoatASiNP also displayed substantial capacity drop after the 40<sup>th</sup> at around  $1000 \text{ mAh g}^{-1}$ . The first cycle efficiency contains irreversible reactions ranging from the SEI formation to the initial structural changes (crystalline to amorphous) of Si [52,53]. CoatASiNP displayed a much lower efficiency that hints at an additional mechanism. From the microscopy images, it appears that the  $\text{Li}^+$  that were able to interact with the SiNP could not all be cycled back during discharge due to the thick C coatings and hence the much lower efficiency. Through cycling, the particles are mainly trapped and encased, restricting the expected expansion of the particles, and less charges are accommodated. Because of the C casing, the CoatASiNP are much more confined than when the SiNP are in the graphene matrix of the composite anode. As a result, there is more capacity degradation. Pristine Si cycled at  $300 \text{ mA g}^{-1}$  [16]) is also depicted in Fig. 14, all composites clearly show better cycling performance even with higher current densities.

The initial capacity displayed by CoatBSiNP ( $3400 \text{ mAh g}^{-1}$ ) is higher than what is expected from a material that is 50% (w/w) Si. This is due to the high surface area of the particles [15]. The efficiency

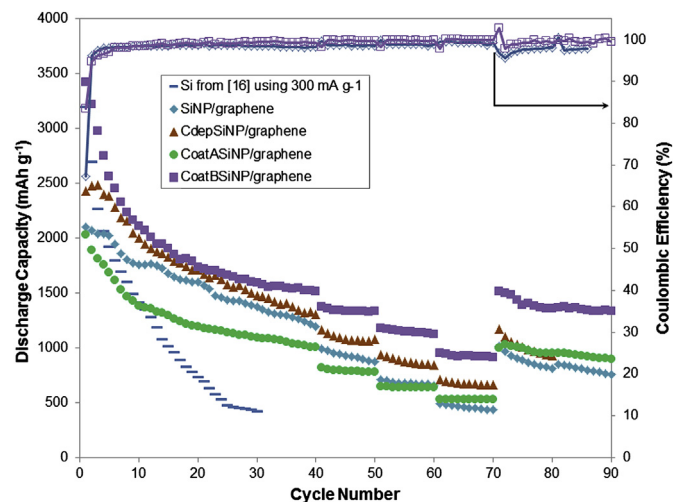


**Fig. 14.** Cycling performance CoatASiNP and CoatBSiNP applied within a composite anode, compared with the unmodified particle and Si [16], using varying current densities.

( $\sim 87\%$ ) is the highest compared to the initial runs of the other two anodes and immediately achieves  $\sim 99\%$  after the second cycle. Such high value can be attributed to the N-containing C coating of the particles, which may provide a stable SEI (compared to the SEI with bare SiNP) and possibly a less obstructed charge diffusion pathway to the SiNP. However, as cycles happen, a high degree of capacity fading is very obvious. Although the discharge capacity is high ( $1730 \text{ mAh g}^{-1}$ ), the drop is almost 50% of the first cycle after 20 cycles. During the second 20 cycles, the capacity ( $\sim 1500 \text{ mAh g}^{-1}$ ) has stabilized. The huge capacity drop can be explained as follows: since the coating is relatively thin, a large number of charges can reach to alloy with Si. As the electrochemical reaction takes place, the SiNP expands while the coating buffers some of the stresses involved. However, at high enough expansions some particles can create void spaces between particles and in the graphene matrix (between sheets) resulting in the disconnection of other particles from the conduction network. Also, coating rupture can happen and expose the particles to the electrolyte. The resulting progressive formation of the unstable SEI on Si with cycling increases electrode resistance. The combination of these occurrences is the likely reason why the magnitude of decay with CoatBSiNP is the greatest. Nonetheless, the capacity stabilization suggests that the particle protection using N-containing C coating is still effective. After the transformations have occurred and the irreversible reactions have been consumed, a stabilized SiNP-coating system is achieved.

At higher rates of cycling, the rate performance of CoatASiNP is improving compared with the bare particles. The observed capacity after the 70<sup>th</sup> cycle is 53% ( $530 \text{ mAh g}^{-1}$ ) of the last capacity using  $500 \text{ mA g}^{-1}$ . The control composite shows only 36% ( $440 \text{ mAh g}^{-1}$ ) of its 40<sup>th</sup> cycle. This indicates that even if the hard C coating restricts the SiNPs, the added benefit of the hard C coating is still better for high rate cycling than having just plain SiNP. The improvements were further amplified with the carbonized PAN coating, displaying 61% ( $920 \text{ mAh g}^{-1}$ ) of its stable  $1500 \text{ mAh g}^{-1}$  while using  $2500 \text{ mA g}^{-1}$  current density. The high rate cyclability of CoatBSiNP is due to both the particle protection given by the N-containing C coating as well as its improved conductivity and charge transfer at the interface [51]. This provides a stable SEI even at high rates of cycling. After reverting back to using  $500 \text{ mA g}^{-1}$  (cycle 71 onwards), CoatBSiNP still achieved the same capacity as before ( $1500 \text{ mAh g}^{-1}$ ) while only displaying very minimal degradation. A N-containing C coating protects the particles and exhibits stable cycling in both low

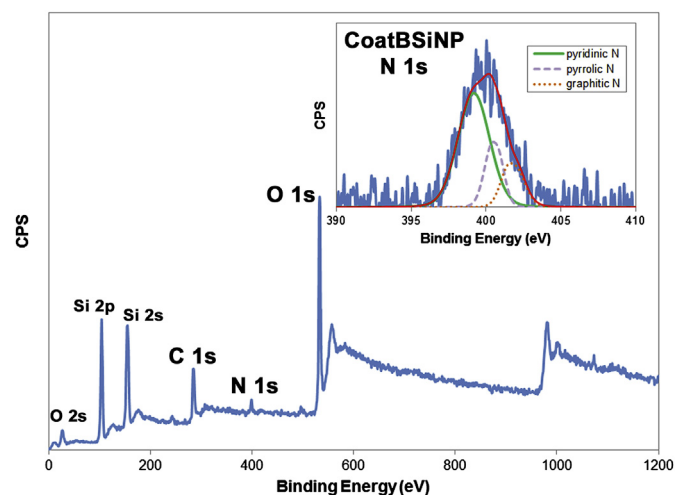


**Fig. 13.** XPS spectra of CoatBSiNP before the composite reduction. Inset: High resolution N 1s spectra showing the binding configurations.

and high current density rates, the best compared to the other coating configurations. All these observed performance improvements emulate the earlier discussed improvements brought by nitriding graphene anodes. With this, the combination of both N-containing graphene and C coating on Si will be investigated as the next generation of composite anode materials. Likewise, rate capability improvement studies with special focus on electrode thickness optimization will be prioritized.

In summary, the graphene sheet size and the resulting level of disorder (once made into an anode material) highly influence the electrochemical performance of a graphene anode material. Likewise, the introduction of ample amount of N within the graphene structure results in both increased capacity and rate capability. SiNP protection through the use of C-based coatings improves the cycling performance of the composite anode material; the best improvements were achieved using N-containing C coating.

#### 4. Conclusions

Subjecting graphite materials with varied flake sizes to Hummers' method (and sonics) can produce graphene anode materials with controlled sheet sizes ranging from 238 to 113 nm. Reactive edge sites became more predominant as sheet size decreases, and an anode containing 238 nm (graphene A) possesses a balance these aspects which led to 240 (at low rate) and 120 mAh g<sup>-1</sup> (at higher rate) outputs. Nitriding the standalone graphene anode through thermal vapor deposition yielded increasing N content with increasing reaction temperature, and the N configuration is likewise temperature dependent. The graphene structure containing around 5.97% (w/w) N is comprised of three binding configurations: pyridinic (72.10%), pyrrolic (22.40%) and graphitic (5.50%). This composition, which was highly influenced by the pyridine-like N, increased the defect and vacancy sites for Li hosting, improved conductivity and stabilized the SEI provided substantially higher capacity at both low (360 mAh g<sup>-1</sup>) and high (215 mAh g<sup>-1</sup>) cycling rates than pristine graphene. Carbon coating schemes to protect the SiNP reveal that the protection should be conforming with the particle at the same time adapting to the expected volume expansion. The developed PAN-based coating resulted in a C coating containing 2.20% N (comprised of 63.20% pyridinic N) which provides intimate contact to the particle. The coating scheme permitted an observed a stable capacity of 1500 mAh g<sup>-1</sup> during low rate cycles and 920 mAh g<sup>-1</sup> at faster cycling. The improved capacity retention and rate capability were obtained by protecting the SiNPs from detrimental SEI and side reactions. Similar to the effect in graphene, the N content improved the conducting network of the particles to enhance the rate capability. Proper control of the modification techniques could potentially offer better overall performance that is much needed by LIBs to properly address current and future performance demands.

#### Acknowledgments

Financial support from the Department of Energy (Grant DE-EE0002106) for this research is gratefully acknowledged.

#### References

- [1] M.N. Obrovac, L. Christensen, *Electrochem. Solid State Lett.* 7 (2004) A93–A96.
- [2] J.M. Tarascon, M. Armand, *Nature* 414 (2001) 359–367.
- [3] J. Graetz, C.C. Ahn, R. Yazami, B. Fultz, *Electrochem. Solid State Lett.* 6 (2003) A194.
- [4] J.P. Maranchi, A.F. Hepp, P.N. Kumta, *Electrochem. Solid State Lett.* 6 (2003) A198.
- [5] S. Bourderau, T. Brousse, D.M. Scheich, *J. Power Sources* 81–82 (1999) 233–236.
- [6] T.L. Kulova, A.M. Skundin, Y.V. Pleskov, E.I. Terukov, O.I. Kon'kov, *J. Electroanal. Chem.* 600 (2007) 217–225.
- [7] C.K. Chan, H. Peng, G. Liu, K. McIlwrath, X.F. Zhang, R.A. Huggins, Y. Cui, *Nat. Nanotechnol.* 3 (2008) 31–35.
- [8] C.K. Chan, R. Ruffo, S.S. Hong, R.A. Huggins, Y. Cui, *J. Power Sources* 189 (2009) 34–39.
- [9] K. Peng, J. Jie, W. Zhang, S.T. Lee, *Appl. Phys. Lett.* 93 (2008) 0331051–0331053.
- [10] M.H. Park, M.G. Kim, J. Joo, K. Kim, J. Kim, S. Ahn, Y. Cui, J. Cho, *Nano Lett.* 9 (2009) 3844–3847.
- [11] H. Kim, B. Han, J. Choo, J. Cho, *Angew. Chem. Int. Ed.* 47 (2008) 10151–10154.
- [12] H.C. Shin, J.A. Corno, J.L. Gole, M. Liu, *J. Power Sources* 139 (2005) 314–320.
- [13] D.K. Kang, J.A. Corno, J.L. Gole, H.C. Shin, *J. Electrochem. Soc.* 155 (2008) A276–A281.
- [14] H. Kim, M. Seo, M.H. Park, J. Cho, *Angew. Chem.* 122 (2010) 2192–2195.
- [15] J.K. Lee, K.B. Smith, C.M. Hayner, H.H. Kung, *Chem. Commun.* 46 (2010) 2025–2027.
- [16] H. Xiang, K. Zhang, J.Y. Lee, C. Zou, X. Chen, J. Wu, *Carbon* 49 (2011) 1787–1796.
- [17] S.L. Chou, J.Z. Wang, M. Choucair, H.K. Liu, J.A. Stride, S.X. Dou, *Electrochem. Commun.* 12 (2010) 303–306.
- [18] N. Liu, H. Wu, M.T. McDowell, Y. Yao, C. Wang, Y. Cui, *Nano Lett.* 12 (2012) 3315–3321.
- [19] H.M. Jeong, S.Y. Lee, W.H. Shin, J.H. Kwon, A. Shakoor, T.H. Hwang, S.Y. Kim, B.S. Kong, J.S. Seo, Y.M. Lee, J.K. Kang, J.W. Choi, *RSC Adv.* 2 (2012) 4311–4317.
- [20] X. Zhou, Y.X. Yin, A.M. Cao, L.J. Wan, Y.G. Guo, *ACS Appl. Mater. Interfaces* 4 (2012) 2824–2828.
- [21] T.H. Hwang, Y.M. Lee, B.S. Kong, J.K. Seo, J.W. Choi, *Nano Lett.* 12 (2012) 802–807.
- [22] B.S. Lee, S.B. Son, K.M. Park, J.H. Seo, S.H. Lee, I.S. Choi, K.H. Oh, W.R. Yu, *J. Power Sources* 206 (2012) 267–273.
- [23] Y. Hernandez, V. Nicolosi, M. Lotya, F.M. Blighe, Z. Sun, S. De, I.T. McGovern, B. Holland, M. Byrne, Y.K. Gun'ko, J.J. Boland, P. Niraj, G. Duesberg, S. Krishnamurthy, R. Goodhue, J. Hutchison, V. Scardaci, A.C. Ferrari, J.N. Coleman, *Nat. Nanotechnol.* 3 (2008) 563–568.
- [24] F. Banhart, P.M. Ajayan, *Nature* 382 (1996) 433.
- [25] M. Liang, L. Zhi, *J. Mater. Chem.* 19 (2009) 5871–5878.
- [26] D. Pan, S. Wang, B. Zhao, M. Wu, H. Zhang, Y. Wang, Z. Jiao, *Chem. Mater.* 21 (2009) 3136–3142.
- [27] O. Yamamoto, Y. Takeda, N. Imanishi, in: *The Electrochemical Society*, Pennington, NJ, 1993, p. 302.
- [28] H. Wang, C. Zhang, Z. Liu, L. Wang, P. Han, H. Xu, K. Zhang, S. Dong, J. Yao, G. Cui, *J. Mater. Chem.* 21 (2011) 5430–5434.
- [29] D. Geng, S. Yang, Y. Zhang, J. Yang, J. Liu, R. Li, T. Sham, X. Sun, S. Knights, *Appl. Surf. Sci.* 257 (2011) 9193–9198.
- [30] D. Deng, X. Pan, L. Yu, Y. Cui, Y. Jiang, J. Qi, W. Li, Q. Fu, X. Ma, Q. Xue, G. Sun, X. Bao, *Chem. Mater.* 23 (2011) 1188–1193.
- [31] X. Li, D. Geng, Y. Zhang, X. Meng, R. Li, X. Sun, *Electrochem. Commun.* 13 (2011) 822–825.
- [32] D. Aurbach, A. Nimberger, B. Markovsky, E. Levi, E. Sominski, A. Gedanken, *Chem. Mater.* 14 (2002) 4155–4163.
- [33] A.A. Arie, W. Chang, J.K. Lee, *J. Solid State Electrochem.* 14 (2010) 51–56.
- [34] B. Saha, G.C. Schatz, *J. Phys. Chem. B* 116 (2012) 4684–4692.
- [35] Z. Liu, D. Lu, Z. Guo, *Appl. Catal. A* 118 (1994) 163–171.
- [36] M.H. Park, K. Kim, J. Kim, J. Cho, *Adv. Mater.* 22 (2010) 415–418.
- [37] N.I. Kovtyukhova, P.J. Ollivier, B.R. Martin, T.E. Mallouk, S.A. Chizhik, E.V. Buzaneva, A.D. Gorchinskiy, *Chem. Mater.* 11 (1999) 771–778.
- [38] S. Chen, P. Chen, M. Wu, D. Pan, Y. Wang, *Electrochem Commun.* 12 (2010) 1302–1306.
- [39] S. Iwamura, H. Nishihara, T. Kyotani, *J. Phys. Chem. C* 116 (2012) 6004–6011.
- [40] Z. Zhu, Z. Liu, Y. Gu, *Fuel* 76 (1997) 155–163.
- [41] C.V. Rao, A.L.M. Reddy, Y. Ishikawa, P.M. Ajayan, *Carbon* 49 (2011) 936.
- [42] P. Lian, X. Zhu, S. Liang, Z. Li, W. Yang, H. Wang, *Electrochim. Acta* 55 (2010) 3909–3914.
- [43] E.J. Yoo, J. Kim, E. Hosono, H. Zhou, T. Kudo, I. Honma, *Nano Lett.* 8 (2008) 2277–2282.
- [44] R. Fong, U.V. Sacken, J.R. Dahn, *J. Electrochem. Soc.* 137 (1990) 2009–2013.
- [45] H. Habazaki, M. Kiri, M. Hayashi, H. Konno, *Mater. Chem. Phys.* 105 (2007) 367–372.
- [46] J. Luo, X. Zhao, J. Wu, H. Jang, H. Kung, J. Huang, *J. Phys. Chem. Lett.* 3 (2012) 1824–1829.
- [47] C. Ma, X. Shao, D. Cao, *J. Mater. Chem.* 22 (2012) 8911–8915.
- [48] P.H. Matter, L. Zhang, U.S. Ozkan, *J. Catal.* 239 (2006) 83–96.
- [49] N.A. Kaskhedikar, J. Maier, *Adv. Mater.* 21 (2009) 2664–2680.
- [50] Y. Wu, S. Fang, W. Ju, Y. Jiang, *J. Power Sources* 70 (1998) 114–117.
- [51] L. Zhao, Y. Hu, H. Li, Z. Wang, L. Chen, *Adv. Mater.* 23 (2011) 1385–1388.
- [52] H. Li, X. Huang, L. Chen, G. Zhou, Z. Zhang, D. Yu, Y.J. Mo, N. Pei, *Solid State Ionics* 135 (2000) 181–191.
- [53] L.F. Cui, R. Ruffo, C.K. Chan, H. Peng, Y. Cui, *Nano Lett.* 9 (2009) 491–495.